Editors' Suggestion

Numerical method for modeling photosynthesis of algae on pulsing soft corals

Matea Santiago [1,*] Kevin A. Mitchell [2,†] and Shilpa Khatri [3,‡]
[1]Department of Mathematics, University of Arizona, Arizona 85711, USA
[2]Department of Physics, University of California, Merced, California 95343, USA
[3]Department of Applied Mathematics, University of California, Merced, California 95343, USA

(Received 9 February 2021; accepted 1 February 2022; published 31 March 2022)

This paper presents a numerical method to study the pulsing behavior of soft corals. Evidence indicates that the pulsing behavior of soft corals in the family Xeniidae facilitates photosynthesis of their symbiotic algae. One way to investigate this complex behavior is through mathematical modeling and numerical simulations. The immersed boundary method is used to model the interaction of the tentacles with the surrounding fluid. The flow is then coupled with a photosynthesis model. The photosynthesis is modeled by advecting and diffusing oxygen, the byproduct of photosynthesis, where the coral tentacles act as a moving source of the oxygen. This study develops a methodology for solving a partial differential equation with boundary conditions on a moving immersed elastic boundary. In this study, the Reynolds and Péclet numbers are varied in the simulations to gain an understanding of how these parameters affect the mixing and photosynthesis. The mixing is quantified using both the fluid flow and oxygen concentration dynamics. The results show that for the biologically relevant Péclet number, the fluid dynamics significantly affect the photosynthesis and that the biologically relevant Reynolds number is advantageous for mixing and photosynthesis.

DOI: 10.1103/PhysRevFluids.7.033102

I. INTRODUCTION

The mechanics of moving organisms, including flight and swimming, has been of interest to the scientific community for many years [1–5]. The knowledge gained from studying the motion of organisms has often been applied to engineering challenges. The mechanics of insect flight has been studied to understand lift [6] and improve the efficiency of drone flight [7]. Numerical and experimental studies of aquatic animal locomotion have led to insights in renewable energy [8], designing underwater and above-water vehicles [9], and swimming efficiency [10,11]. The ability to study these dynamics analytically and experimentally is limited due to these system's complexity. Computational simulations can be used to gain further insight into various properties of the system [2]. The studies mentioned above have focused on mechanics relating to locomotion. This paper will focus on the computational simulations of pulsing soft corals in the family Xeniidae which are sessile. Their pulsing motion mixes the surrounding fluid rather than for transportation.

This mixing in the fluid due to coral pulsing can facilitate waste removal and carbon dioxide access for the symbiotic photosynthetic algae, providing the coral with additional energy. There are numerous examples in which the interaction of organisms, fluid flow, and chemical concentrations

*malvarado27@ucmerced.edu
†kmitchell@ucmerced.edu
‡skhatri3@ucmerced.edu

 ©2022 American Physical Society

play a role in ecological systems. The role of fluid flow has been investigated in different types of feeding and nutrient access [12–15]. Chemosensing is important in marine life. For example, crabs sniff by using their olfactory antennules to capture odorants from surrounding fluid to extract information from their environment [16–18]. Chemotaxis processes and chemoattractants have also been studied in bacteria [19–21], phytoplankton [22], sperm, and spawning [23–26]. The dynamics of the dissolved gases that are the reactants and byproducts of the symbiotic algae photosynthesis coupled with the fluid flow of the pulsing coral are investigated in this paper. Photosynthesis is a process where plants and other organisms obtain energy through sunlight and gases rather than consuming other organisms. In photosynthesis, sunlight, carbon dioxide, and water are converted through metabolic processes into the energy source, glucose, and the byproduct oxygen.

The interaction of fluid flow and dissolved gases involved in photosynthesis is also more broadly a topic of interest. Fluid mixing is necessary for efficient photobioreactors to cultivate microalgae, which can be used as a biofuel [27]. Fluid flow and transport of oxygen and carbon dioxide have been found to be important for photosynthesis of benthic marine autotrophs [28]. In particular, the effects of fluid flow on photosynthesis and mass transfer around stony corals have been well studied [29–31]. In this work, the interactions between the pulsing flow and the photosynthesis of the symbiotic algae on the tentacles of the soft corals in the family Xeniidae are modeled.

Soft corals are known to be more resistant to ocean acidification than stony corals, which make up the structure of coral reefs [32]. As climate change progresses, understanding the ecological dynamics of coral reefs is vital. This work seeks to bring insight into the energy source for these soft corals. The purpose of the pulsing motion was thought to help with food capture. However, they are rarely found with food in their gastric cavities [33,34]. These soft corals are one of the only known sessile animals who move with such an energetically expensive behavior [35]. Experimental studies have shown increased photosynthesis in the symbiotic algae of soft corals that are pulsing compared to stationary corals. It is believed that the coral's main source of energy is through this symbiotic relationship rather than through filter-feeding. During photosynthesis, chemical energy is synthesized from carbon dioxide with oxygen as a byproduct. These experimental studies have suggested that photosynthesis is an oxygen-limited process. The study found that artificially heightened oxygen levels in the fluid tank resulted in less photosynthesis by the symbiotic algae [35]. Numerical studies simulating the flow around pulsing soft corals [36,37] focus on analyzing this flow. This is the first study to examine the interaction of fluid flow around the pulsing corals with the photosynthesis of the symbiotic algae.

To capture the characteristics of the fluid flow in varying regimes, the Reynolds number, the ratio of inertial to viscous forces, and the Péclet number, the ratio of advection to diffusion, are used. By varying the Reynolds and Péclet numbers in the simulations, the role of fluid inertia in response to the coral pulsing and the diffusivity of the oxygen is studied and quantified. In other studies and applications, varying the Reynolds number has given insight into the behavior of fluid flow at different length scales, velocities, and fluid viscosities [38–41] and varying the Péclet number has given insight into the dynamics of chemical concentrations being advected at different speeds, different length scales, and differing diffusivities [17,42–46]. In this paper, we vary the Reynolds and Péclet numbers to understand how these dimensionless parameters affect the mixing due to the fluid dynamics around the pulsing soft coral and the resulting photosynthesis of their symbiotic algae. The size and pulsing frequency of the corals modify these parameters. By varying the Reynolds and Péclet numbers independently, we explore the relative importance of different parameter regimes and why the corals may have evolved to their current state and behaviors.

This paper will present a model and numerical method to study the pulsing behavior of a coral polyp and the photosynthesis of the symbiotic algae. This work has two components, the first is modeling the polyp movement and the resulting fluid flow, which is modeled using the immersed boundary method [47]. The second is coupling the fluid flow with the production of oxygen around the pulsing polyp, which will be modeled using the advection-diffusion equation coupled with the fluid-structure interaction. The immersed boundary method is a front-tracking method that has been used to model other biomechanical problems. In particular, it has been used extensively to model

TABLE I. Physical parameters of the soft coral Xeniidae.

Parameter	Description	Value	Units
L	Tentacle length	0.4070	cm
γ	Pulsation frequency	0.5286	s^{-1}
ν	Kinematic fluid viscosity	0.01	cm^2s^{-1}
D	Diffusion coefficient	2×10^{-5}	cm^2s^{-1}
Re	Reynolds number	8.756	

elastic-body fluid interactions in physiology [48–52] and aquatic animal locomotion [53,54]. To model photosynthesis, we represent dissolved oxygen as a concentration in the fluid governed by the advection-diffusion equation. As the tentacles move through the fluid, they produce oxygen. Thus, modeling a moving boundary as a source of a chemical concentration is an important component of this work. We present a numerical method to address this challenge.

In the following, the mathematical models are presented in Sec. II, the numerical methods and their validation are discussed in Sec. III, and the results are presented in Sec. IV. This is followed by the discussion and conclusions of the results in Sec. V.

II. MATHEMATICAL MODELS

The first component in this work is to model the fluid-structure interaction of the pulsing tentacles of the coral polyp. The immersed boundary (IB) method is used to model this moving elastic body, the coral polyp, and the resulting fluid flow [48]. The IB method allows for the flow to be solved computationally on a uniform Cartesian grid around complex, moving, immersed elastic boundaries that are described using Lagrangian coordinates. This allows for straightforward computations without needing complex moving body-fitted grids. The IB method has been well studied numerically, [55–59], extended [60–63], and analyzed [64,65].

The fluid flow is modeled on a two-dimensional rectangular domain, $\underline{x} = (x_1, x_2) \in \Omega$. The flow velocity, $\underline{u}(\underline{x}, t) = (u_1, u_2)$, and pressure, $p(\underline{x}, t)$, are solved using the Navier-Stokes equations for an incompressible, viscous fluid in a periodic channel initially at rest,

$$\frac{\partial \underline{u}}{\partial t} + \underline{u} \cdot \nabla \underline{u} + \nabla p = \frac{1}{\mathrm{Re}} \nabla^2 \underline{u} + \underline{f}, \tag{1}$$

$$\nabla \cdot \underline{u} = 0. \tag{2}$$

The velocity has homogeneous Dirichlet boundary conditions at the top and bottom of the domain and periodic boundary conditions at the sides of the domain. The periodic boundary condition accounts for the fact that these corals live in colonies. The homogeneous Dirichlet boundary conditions are a simplifying modeling choice. The domain is chosen to be large enough so that the boundary conditions do not affect the flow dynamics around the coral. The dimensionless Reynolds number is defined as $\mathrm{Re} = \frac{L^2\gamma}{\nu}$, where L is the characteristic length, γ is the characteristic frequency, and ν is the kinematic viscosity. In this study, the characteristic length is the length of a coral polyp tentacle and the characteristic frequency is the frequency of the coral pulsation. These values are provided in Table I. The force per area, $\underline{f}(\underline{x}, t)$, is the force of the tentacles on the fluid which couples the fluid flow to the immersed boundary.

Two additional interaction equations couple the elastic boundary, the coral tentacles, and the fluid. The force defined on the fluid, $\underline{f}(\underline{x}, t)$, is extrapolated from the force of the boundary on the fluid, $\underline{F}(s, t)$, which is defined on the Lagrangian boundary,

$$\underline{f}(\underline{x}, t) = \int_0^{\ell} \underline{F}(s, t)\delta[\underline{x} - \underline{X}(s, t)]ds. \tag{3}$$

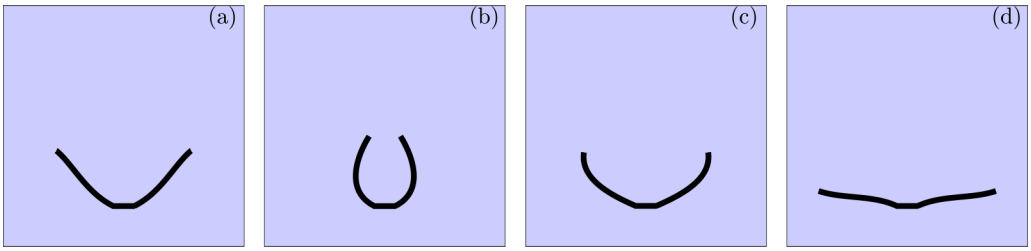

FIG. 1. This figure shows the 2D model corals at (a) 10%, (b) 30%, (c) 50%, and (d) 80% through a pulse.

Further, the velocity of the immersed boundary is interpolated from the velocity of the surrounding fluid,

$$\frac{\partial \underline{X}}{\partial t}(s,t) = \underline{U}(s,t) = \underline{u}[\underline{X}(s,t)] = \int_{\Omega} \underline{u}(\underline{x},t)\delta[\underline{x} - \underline{X}(s,t)]d\underline{x}. \tag{4}$$

In these equations, the boundary position is given by $\underline{X}(s,t)$ as a function of the arclength s defined from 0 to ℓ and $\underline{x}$ is the position in the fluid.

The force of the boundary on the fluid is used to prescribe the motion of the pulsing coral. Tether points are used to prescribe this motion. They do not interact with the fluid; instead, they move in a defined way to give the desired pulsing behavior. Then, the force is computed as

$$\underline{F}(s,t) = \kappa_T[\underline{X}_T(s,t) - \underline{X}(s,t)] + \kappa_d[\underline{U}_T(s,t) - \underline{U}(s,t)] \tag{5}$$

for the position of the tether points, $\underline{X}_T(s,t)$, spring constant, κ_T, velocity of the tether points, $\underline{U}_T$, and damping coefficient κ_d [63].

The tether point positions, $\underline{X}_T(s,t)$, determine how the corals pulse in the numerical simulations. These positions are determined from experimental data [36]. The experimental data was collected assuming the motion of all eight tentacles is identical and each tentacle moves radially. To model the coral movement in two dimensions, two tentacles are included, and it is assumed that the motion of each tentacle is a reflection of the other; see Fig. 1. Figure 1(a) shows the closing phase, Figs. f1(b) and 1(c) show the opening phase, and Fig. 1(d) shows the resting phase. More details of this prescribed kinematic motion are provided in Appendix A.

The main goal of this paper is to model photosynthesis coupled to the fluid-structure interaction of a pulsing coral polyp. To model the photosynthesis of the symbiotic algae on the coral tentacle, we consider the coral tentacles as a source of oxygen and a sink of carbon dioxide. In this formulation only the byproduct of photosynthesis, oxygen, is tracked since it is assumed that this process is oxygen-limited [35].

The concentration dynamics of oxygen are modeled using the advection-diffusion equation with an extra source term, coupled to the immersed boundary equations, Eqs. (1)–(5),

$$c_t + \underline{u} \cdot \nabla c = \frac{1}{\mathrm{Pe}}\nabla^2 c + \int_{\Gamma} \tilde{f}(s,t)\delta[\underline{x} - \underline{X}(s,t)]d\underline{s}. \tag{6}$$

Here, $c(\underline{x},t)$ is the oxygen concentration and $\underline{u}(\underline{x},t)$ is the fluid velocity solved for in Eqs. (1) and (2). The concentration has no-flux boundary conditions at the top and bottom of the domain and periodic boundary conditions at the sides of the domain. The dimensionless Péclet number is defined as $\mathrm{Pe} = \frac{L^2\gamma}{D}$, where the characteristic length L, frequency γ, and diffusion coefficient D are given in Table I. The last term in Eq. (6) models the tentacle as a source of oxygen, where $\tilde{f}(s,t)$ is the photosynthesis model chosen. This immersed boundary delta function approach is based on the modeling by Chen and Lai for surfactants that are adsorbed and desorbed from a bulk fluid to an interface [66]. This approach has also been used as point sources of concentration to model bioconvection of motile bacteria [67] and cell aggregation relating to constructing biofilms [21]. It is

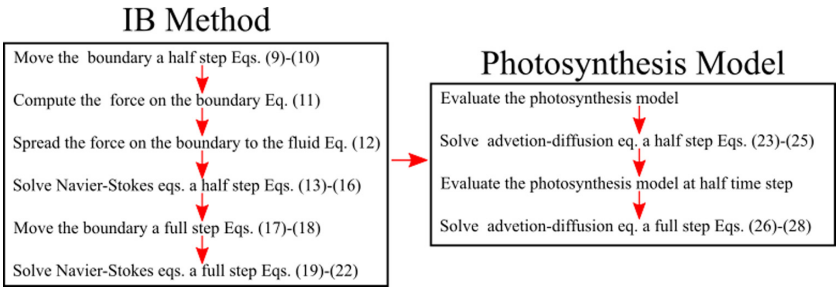

FIG. 2. Schematic of the numerical time-stepping scheme for the coupled immersed boundary (IB) method and photosynthesis model.

a natural approach to coupling advection and diffusion of a quantity with a fluid-structure interaction when using the immersed boundary method.

We choose an oxygen-limited model for photosynthesis,

$$\tilde{f}(s,t) = \kappa[1 - C(s,t)], \tag{7}$$

where

$$C(s,t) = \int_{\Omega} c(\underline{x},t)\delta[\underline{x} - \underline{X}(s,t)]d\underline{x}. \tag{8}$$

Equation (8) is the oxygen concentration that has been interpolated to the location of the tentacles. It gives a measure of how much oxygen is present locally around the tentacles. κ is the desorption rate of the oxygen from the tentacles to the fluid. The amount of photosynthesis that occurs and the amount of oxygen byproduct produced is dependent only on the amount of oxygen present locally. Since this model does not depend on carbon dioxide there is no need to model and track the carbon dioxide concentration. Throughout this paper, we refer to this model as the oxygen-limited model.

We also consider another model for the purpose of analyzing and validating the methodology. The constant model assumes $\tilde{f}(s,t) = \kappa$, where a constant amount of oxygen is produced at all times. For both models, there is no initial concentration present in the domain. We also considered a model with no sources or sinks $\tilde{f}(s,t) = 0$ and with an initial condition of a Gaussian function defined along the tentacles. The dynamics for this system were found to not capture the photosynthesis dynamics and are omitted from this work. The modeling introduced by Eq. (6) is necessary to capture the photosynthesis dynamics coupled to the pulsing motion and fluid flow.

III. NUMERICAL METHODS

We solve the coupled equations presented in the previous section using numerical methods. First, the numerical discretization of the IB method for the fluid flow is discussed, and then the discretization of the advection-diffusion equation for the oxygen concentration dynamics is presented. The time stepping for the entire system is outlined in Fig. 2.

There are three components in discretizing the IB method: discretizing the Navier-Stokes equations, the immersed boundary, and the interaction equations which provide the coupling between the two. A projection method is used to solve the Navier-Stokes equations, Eqs. (1) and (2). Projection methods, first developed by Chorin [68], are a standard finite difference approach to solving the Navier-Stokes equations. In this work, the rotational form of the incremental pressure-correction method developed by Timmermans *et al.* is used [69]. The rotational form avoids prescribing artificial numerical boundary conditions for the pressure. In a periodic channel, this method has been shown to be second-order convergent for the velocity and pressure [70] and has been used with other immersed boundary problems [71,72].

The fluid grid is discretized on a marker and cell grid [73] with a mesh width h and time step Δt. Standard centered finite differences are used for the discrete gradient, ∇_h, and discrete Laplacian, ∇_h^2, operators. The immersed boundary is discretized with N points separated by $\Delta s \approx \frac{h}{2}$ which is a necessary numerical constraint [47]. The position of the kth point at time t^n, on the boundary curve representing the coral tentacles is denoted $\underline{X}_k^n$ and the position of the kth tether point at the same time is similarly denoted $\underline{X}_{Tk}^{\ n}$.

Choosing a method to compute the force, $\underline{f}$, is nontrivial [74] since the force is dependent on the tentacle location. We choose to handle it explicitly and solve the fully coupled system by taking two half time steps. In the first step, the velocity at times t^n and $t^{n-1/2}$ and the pressure and boundary position at time t^n are used to advance the solution to the system to time $t^{n+1/2}$.

First, the velocity $\underline{U}^n$ on the boundary $\underline{X}^n$ is evaluated using the trapezoidal rule and a regularized delta function, δ_h to discretize Eq. (4),

$$\underline{U}_k^n = \sum_{ij} \underline{u}_{ij}^n \delta_h\left(\underline{X}_k^n - \underline{x}_{ij}\right) h^2, \tag{9}$$

where the ij subscripts denote the Cartesian grid points on the fluid grid. The boundary is then advanced a half time step using forward Euler,

$$\underline{X}_k^{n+1/2} = \underline{X}_k^n + \frac{\Delta t}{2} \underline{U}_k^n. \tag{10}$$

The force, $\underline{F}^{n+1/2}$ is computed on this boundary, $\underline{X}^{n+\frac{1}{2}}$, using Eq. (5),

$$\underline{F}_k^{n+1/2} = \kappa_T\left(\underline{X}_{Tk}^{\ n+1/2} - \underline{X}_k^{n+1/2}\right) + \kappa_d\left(\frac{\underline{X}_{Tk}^{\ n+1/2} - \underline{X}_{Tk}^{\ n-1/2}}{\Delta t} - \underline{U}_k^n\right), \tag{11}$$

and then spread to the fluid grid to evaluate $\underline{f}^{n+\frac{1}{2}}$, using the trapezoidal rule for Eq. (3),

$$\underline{f}_{ij}^{n+1/2} = \sum_{k=1}^{N-1} \left[\underline{F}_k^{n+1/2} \delta_h\left(\underline{X}_k^{n+1/2} - \underline{x}_{ij}\right) + \underline{F}_{k+1}^{n+1/2} \delta_h\left(\underline{X}_{k+1}^{n+1/2} - \underline{x}_{ij}\right)\right] \frac{\Delta s}{2}. \tag{12}$$

Then, the Navier-Stokes equations, Eqs. (1) and (2), are solved at time $t^{n+1/2}$ for fluid velocity $\underline{u}^{n+\frac{1}{2}}$ and pressure $p^{n+\frac{1}{2}}$ using the force $\underline{f}^{n+\frac{1}{2}}$. First, a second-order backwards difference formula is used to advance Eq. (1) a half time step for an intermediate velocity field $\underline{\tilde{u}}^{n+1/2}$ at time $t^{n+1/2}$ using the velocities, $\underline{u}^n$ and $\underline{u}^{n-1/2}$ at times t^n and $t^{n-1/2}$, respectively, and the pressure at time t^n, p^n,

$$\begin{aligned} &\frac{1}{\Delta t}(3\underline{\tilde{u}}^{n+1/2} - 4\underline{u}^n + \underline{u}^{n-1/2}) + 2(\underline{u}^n \cdot \nabla_h)\underline{u}^n - (\underline{u}^{n-1/2} \cdot \nabla_h)\underline{u}^{n-1/2} \\ &\quad - \frac{1}{\mathrm{Re}} \nabla_h^2 \underline{\tilde{u}}^{n+1/2} + \nabla_h p^n = \underline{f}^{n+1/2}. \end{aligned} \tag{13}$$

Using the intermediate velocity, $\underline{\tilde{u}}^{n+1/2}$, a Poisson equation is then solved for the auxiliary function $\psi^{n+1/2}$,

$$\nabla_h^2 \psi^{n+1/2} = \frac{3}{\Delta t} \nabla_h \cdot \underline{\tilde{u}}^{n+1/2}, \tag{14}$$

with mixed homogeneous Neumann (on the top and bottom of the rectangular domain) and periodic (on the sides of the rectangular domain) boundary conditions. Finally, the auxiliary function, $\psi^{n+1/2}$, is used to update the pressure and velocity at time $t^{n+1/2}$,

$$p^{n+1/2} = \psi^{n+1/2} + p^n - \frac{1}{\mathrm{Re}} \nabla_h \cdot \underline{\tilde{u}}^{n+1/2}, \tag{15}$$

$$\underline{u}^{n+1/2} = \underline{\tilde{u}}^{n+1/2} - \frac{1}{3} \Delta t \nabla_h \psi^{n+1/2}, \tag{16}$$

which enforces the incompressibility condition, Eq. (2).

In the second step the velocity at times $t^{n+1/2}$ and t^n, and pressure and boundary position at time $t^{n+1/2}$, evaluated in the first step, are used to advance the solution of the coupled system to time t^{n+1} using similar methodology as in the first step. The boundary velocity $\underline{U}^{n+\frac{1}{2}}$ on the boundary $\underline{X}^{n+\frac{1}{2}}$ is computed using the trapezoidal rule, similar to Eq. (9), using the velocity solved for in the previous step, $\underline{u}^{n+\frac{1}{2}}$,

$$\underline{U}_k^{n+\frac{1}{2}} = \sum_{ij} \underline{u}_{ij}^{n+\frac{1}{2}} \delta_h\big(\underline{X}_k^{n+\frac{1}{2}} - \underline{x}_{ij}\big)h^2. \tag{17}$$

The boundary is then advanced a full time step using this velocity,

$$\underline{X}^{n+1} = \underline{X}^n + \Delta t \underline{U}^{n+\frac{1}{2}}. \tag{18}$$

Finally, the Navier-Stokes equations, Eqs. (1) and (2), are solved at time t^{n+1} for fluid velocity $\underline{u}^{n+1}$ and pressure p^{n+1} using the force $\underline{f}^{n+\frac{1}{2}}$ using the same method as in the first step,

$$\frac{1}{\Delta t}(3\tilde{\underline{u}}^{n+1} - 4\underline{u}^{n+1/2} + \underline{u}^n) + 2(\underline{u}^{n+1/2} \cdot \nabla_h)\underline{u}^{n+1/2} - (\underline{u}^n \cdot \nabla_h)\underline{u}^n$$
$$- \frac{1}{\mathrm{Re}}\nabla_h^2 \tilde{\underline{u}}^{n+1} + \nabla_h p^{n+1/2} = \underline{f}^{n+1/2}, \tag{19}$$

$$\nabla_h^2 \psi^{n+1} = \frac{3}{\Delta t}\nabla_h \cdot \tilde{\underline{u}}^{n+1}, \tag{20}$$

$$p^{n+1} = \psi^{n+1} + p^{n+1/2} - \frac{1}{\mathrm{Re}}\nabla_h \cdot \tilde{\underline{u}}^{n+1}, \tag{21}$$

$$\underline{u}^{n+1} = \tilde{\underline{u}}^{n+1} - \frac{1}{3}\Delta t \nabla_h \psi^{n+1}. \tag{22}$$

Note once again, we have introduced an auxiliary function ψ^{n+1} to enforce the incompressibility condition.

An analytic delta function would not capture the interaction of the fluid grid and the boundary in Eqs. (9), (12), and (17) because the immersed boundary Lagrangian points do not perfectly align with the Cartesian fluid grid. Therefore, a regularized delta function is used at $\underline{x} = (x_1, x_2)$, defined as $\delta_h(\underline{x}) = \delta_h(x_1)\delta_h(x_2)$, where δ_h is a smooth continuous function with bounded support in the form $\delta_h(x) = \frac{1}{h}\phi(\frac{x}{h})$. In this work $\phi(x)$ is defined as

$$\phi(x) = \begin{cases} \frac{1}{4}\big(1 + \cos\big(\frac{x\pi}{2}\big)\big) & |x| \leqslant 2h, \\ 0 & \text{otherwise.} \end{cases}$$

Further details for this choice of $\phi(x)$ are discussed in Peskin [47].

Once the fluid-structure interaction equations are solved, we use the fluid velocity and coral tentacle locations to solve for the oxygen concentration. Strang splitting is used to solve the advection-diffusion equation, Eq. (6) [75]. By using Strang splitting, the advection and diffusion operators are split so that each may be solved using different numerical methods. The forcing term in the advection-diffusion equation involves the concentration dynamics defined on the boundary and therefore solving implicitly would be challenging. A similar approach as used to discretize the IB method is used.

The solution is advanced a half time step to find the concentration solution $c^{n+1/2}$ using c^n to compute $\tilde{f}_k^n$ using either the oxygen-limited model, Eq. (7), or the constant model. In the oxygen-limited model, the trapezoidal rule is used to discretize Eq. (8) to evaluate C_k^n. First, we take a quarter step and solve the advection equation using an explicit upwinding method,

$$c^* = c^n - \frac{\Delta t}{4}\big(\tilde{c_x}^n + u_2^n \tilde{c_y}^n\big). \tag{23}$$

TABLE II. Convergence results for the velocity field. The error and order of convergence is presented in both the L_2 and L_∞ norms for both components of the velocity field, u_1 and u_2.

h	Δt	$\|\|u_{1h}-u_{1h/2}\|\|_2$	Order	$\|\|u_{2h}-u_{2h/2}\|\|_2$	Order	$\|\|u_{1h}-u_{1h/2}\|\|_\infty$	Order	$\|\|u_{2h}-u_{2h/2}\|\|_\infty$	Order
0.0300	2.50×10^{-6}	3.42×10^{-1}	—	4.89×10^{-1}	—	1.72×10^{0}	—	1.04×10^{0}	—
0.0150	1.25×10^{-6}	1.63×10^{-1}	1.06	1.93×10^{-1}	1.34	1.20×10^{0}	0.52	6.11×10^{-1}	1.06
0.0075	6.25×10^{-7}	8.09×10^{-2}	1.01	8.47×10^{-2}	1.19	9.38×10^{-1}	0.35	3.44×10^{-1}	1.01

The discrete derivatives, $\tilde{c_x}$ and $\tilde{c_y}$, are determined using a third order weighted essentially nonoscillatory (WENO) scheme developed by Lui *et al.* [76]. Then, a half time step of Crank-Nicolson, an implicit method, is used to solve the diffusion equation with the source term kept explicit,

$$\frac{c^{**}-c^{*}}{\Delta t}=\frac{1}{\mathrm{Pe}}\nabla_h^2(c^{**}+c^{*})+\sum_{k=1}^{N}\tilde{f}_k^n\delta_h\big(\underline{X}_k^n-\underline{x}_{ij}\big)\Delta s. \tag{24}$$

Then, another quarter time step of the advection equation is used to compute $c^{n+1/2}$,

$$c^{n+1/2}=c^{**}-\frac{\Delta t}{4}\big(u_1^n\tilde{c_x}^{**}+u_2^n\tilde{c_y}^{**}\big). \tag{25}$$

In the second step, $c^{n+1/2}$ is used to find $\tilde{f}_k^{n+1/2}$ which is then used to advance the concentration solution a full time step in a similar manner as in the previous step to find c^{n+1},

$$c^{*}=c^{n}-\frac{\Delta t}{2}\big(u_1^n\tilde{c_x}^{n}+u_2^n\tilde{c_y}^{n}\big), \tag{26}$$

$$\frac{c^{**}-c^{*}}{2\Delta t}=\frac{1}{\mathrm{Pe}}\nabla_h^2(c^{**}+c^{*})+\sum_{k=1}^{N}\tilde{f}_k^{n+1/2}\delta_h\big(\underline{X}_k^{n+1/2}-\underline{x}_{ij}\big)\Delta s, \tag{27}$$

$$c^{n+1}=c^{**}-\frac{\Delta t}{2}\big(u_1^n\tilde{c_x}^{**}+u_2^n\tilde{c_y}^{**}\big). \tag{28}$$

We have advanced the coupled system one time step, solving for the velocity, pressure, and oxygen concentration. We continue to solve over multiple time steps until we reach the desired final time.

A. Convergence studies

To validate the methodology, a convergence study was conducted for a pulsing coral up to final time 0.4, 40% through a pulse on a 3×3 domain. The grid sizes used for the fluid grid are $h=0.03$, 0.015, 0.0075, and 0.00375. The number of points to discretize a tentacle is given by $N=\lceil 2/h\rceil$. The spring constant in Eq. (5) is dependent on the number of immersed boundary points, defined as $\kappa_T=\frac{C_T}{\rho L^3\gamma^2}N^2$ and the damping coefficient in Eq. (5) is dependent on the spring constant, $\kappa_d=C_d\sqrt{\kappa_T}$ [63]. For stability, the time step Δt is dependent on the spring constant, $\Delta t=\frac{\gamma C_t}{\sqrt{\kappa_T}}$ [63]. C_T, C_d, and C_t are constants that need to be empirically chosen. $C_T=100$ is chosen to be as large as necessary, and $C_t=1/\,106.4057$ is chosen to be as small as necessary. $C_d=5$ is chosen to provide damping to the springs for stability. The error at mesh width h, for a quantity Q_h is approximated as $Q_h-Q_{h/2}$.

The convergence results for the velocity field are shown in Table II. We would expect above first order in the L_2 norm and first order in the L_∞ norm for an idealized case assuming Stokes flow and a closed immersed boundary [65,77]. In this work we are using the Navier-Stokes equations on an open immersed boundary. In prescribing the motion of the coral tentacles, there is a large initial acceleration to allow for accuracy of the coral motion. This yields large initial errors in the tether

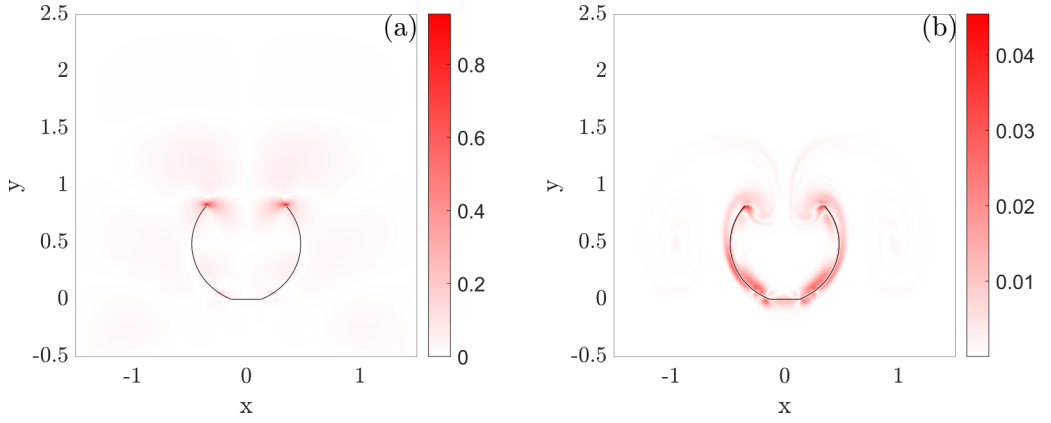

FIG. 3. Error magnitude at time $t = 0.4$ with $h = 0.0075$ for (a) u_1 and (b) c where $\mathrm{Pe} = 400$.

points and thus in the fluid, particularly for a coarse mesh, which is seen in the convergence study. The magnitude of the error for u_1 is shown in Fig. 3 (a). One can see that the L_∞ error is at the tips of the tentacles. However, it is clear that as the grid is refined the method is converging on a solution at approximately the expected order.

A corresponding convergence study was conducted for the concentration dynamics coupled to the flow up to final time 0.4. The velocity fields and boundary positions from the previous study are used so the concentration is solved using the same grid sizes used for the fluid flow, $h = 0.03$, 0.015, 0.0075, and 0.00375. The time step, $\Delta t = \frac{h}{240}$, is significantly larger than for the velocity solution. The smaller time step used for the IB simulations was necessary for the stability of the velocity fields due to the large spring constant, but is not necessary for computing the concentration dynamics. The time step chosen satisfies the CFL condition of the advection equation.

The error and the norms are computed as in the velocity convergence study. The convergence study results for the concentration with $\mathrm{Pe} = 1$ and $\mathrm{Pe} = 400$ are shown in Table III. As the Péclet number increases, the solutions have sharper gradients at the tentacles which slightly degrades the order of convergence observed. The magnitude of the error for c and $\mathrm{Pe} = 400$ is shown in Fig. 3(b). One can see that the large error is around the tentacles. However, we observe that the solution is converging to first order.

To understand what grid sizes need to be used for the simulations, we also need to consider the relative error. In Table IV, the relative error, $\frac{||Q_h - Q_{h/2}||}{||Q_{h/2}||}$, for a quantity Q_h approximated with spatial grid h in the L_2 and L_∞ norm are shown for $\mathrm{Re} = 8$ and $\mathrm{Pe} = 1$ and 400. The relative L_2 error of the velocities are small, 5% or less at the two finest meshes. The relative L_∞ error is decreasing, but still relatively large for the horizontal velocity. However, this error is localized around the tentacles. In the simulations shown in Sec. IV, the spatial grid chosen for the velocity simulations is the intermediate spatial grid $h = 0.015$ and a time step of $\Delta t = 2.666 \times 10^{-6}$. We chose a time step

TABLE III. Convergence results for the concentration field solved using the oxygen-limited source term. The error and order of convergence is presented in both the L_2 and L_∞ norms for $\mathrm{Pe} = 1$ and $\mathrm{Pe} = 400$.

		Pe = 1				Pe = 400			
h	Δt	$\|\|c_h - c_{h/2}\|\|_2$	Order	$\|\|c_h - c_{h/2}\|\|_\infty$	Order	$\|\|c_h - c_{h/2}\|\|_2$	Order	$\|\|c_h - c_{h/2}\|\|_\infty$	Order
0.0300	1.25×10^{-4}	6.30×10^{-4}	—	1.07×10^{-3}	—	2.62×10^{-2}	—	9.87×10^{-2}	—
0.0150	6.25×10^{-5}	3.34×10^{-4}	0.92	7.76×10^{-4}	0.46	1.39×10^{-2}	0.92	6.19×10^{-2}	0.67
0.0075	3.12×10^{-5}	6.65×10^{-5}	2.33	2.32×10^{-4}	1.74	7.26×10^{-3}	0.94	4.54×10^{-2}	0.45

TABLE IV. Relative error for the fluid velocity with Re = 8 and concentration dynamics with Pe = 1 and Pe = 400 using the L_2 and L_∞ norms. The time steps used to compute the velocity and concentration simulations are $\Delta t = h/12000$ and $\Delta t = h/240$, respectively.

h	Re = 8 $\frac{\|u_{1h}-u_{1h/2}\|_2}{\|u_{1h}\|_2}$	$\frac{\|u_{2h}-u_{2h/2}\|_2}{\|u_{2h}\|_2}$	Pe = 1 $\frac{\|c_h-c_{h/2}\|_2}{\|c_h\|_2}$	Pe = 400 $\frac{\|c_h-c_{h/2}\|_2}{\|c_h\|_2}$	Re = 8 $\frac{\|u_{1h}-u_{1h/2}\|_\infty}{\|u_{1h}\|_\infty}$	$\frac{\|u_{2h}-u_{2h/2}\|_\infty}{\|u_{2h}\|_\infty}$	Pe = 1 $\frac{\|c_h-c_{h/2}\|_\infty}{\|c_h\|_\infty}$	Pe = 400 $\frac{\|c_h-c_{h/2}\|_\infty}{\|c_h\|_\infty}$
0.0300	0.099	0.075	0.016	0.227	0.429	0.145	0.032	0.312
0.0150	0.050	0.032	0.009	0.113	0.307	0.089	0.023	0.163
0.0075	0.026	0.014	0.002	0.059	0.253	0.051	0.007	0.107

approximately double that of the time step in the convergence study, as most of the error is due to the spatial discretization and this choice does not significantly modify the results. This allowed for shorter wall-clock times for the simulations.

The relative errors for the concentration are also presented in Table IV. The L_2 and L_∞ errors with Pe = 1 are always less than 4%. As discussed above, the concentration dynamics have much sharper gradients near the tentacles as the Péclet number increases. So the relative L_2 error for Pe = 400 has much larger values for coarse grids but less than 6% for the finest mesh. The relative L_∞ error similarly has large values for the coarse grids but decreases for the finest mesh. In this case, it is clear that we need to use the finest mesh for the larger Péclet numbers, so the finest mesh, $h = 0.0075$, with a time step of $\Delta t = 5.3203 \times 10^{-4}$ was chosen for all the concentration simulations. Again, a larger time was chosen for the simulations since the majority of the error is due to the spatial discretizations. This time step is small enough to achieve less than 5% mass loss. To couple the fluid grid with a coarser mesh to the finer concentration grid, the velocity was interpolated onto the finer mesh using a second-order method.

IV. RESULTS

Numerical simulations and analysis were conducted to study the interplay of the photosynthesis of the symbiotic algae and the fluid flow created by the pulsing soft corals. Fluid flow results are provided in Sec. IV A and analysis of the fluid mixing is provided in Sec. IV B. The periodic steady-state velocity simulations are used to quantify the mixing using a dynamical systems approach. The results of the simulations of the pulsing coral coupled with the photosynthesis model are provided in Sec. IV C. The dynamics are analyzed to understand the role of the mixing in the photosynthesis.

A. Velocity simulations

Here, we present simulations of the fluid flow of the pulsing coral. In these simulations, the Reynolds number is varied, Re = 1, 4, 8, 12, and 16, around the biologically relevant Reynolds number, Re $\approx$ 8. The simulations are run on a 3.75×9 domain. These simulations are run until they reach a quasi-steady-state and are time periodic. For Re = 1, 4, and 8, steady state was achieved by nine pulses and for Re = 12 and 16, steady state was achieved by 24 pulses. A series of snapshots of the velocity field during the ninth pulse for the Re = 8 simulation is shown in Fig. 4.

Average horizontal and vertical velocities on vertical and horizontal lines, respectively, for Re = 1, 8, and 16 at varying distances from the pulsing coral are presented in Fig. 5. Results of the last three pulses of each simulation are presented, denoted by the shading. The vertical dashed black lines indicate the change of phase during each pulse. The first dotted black line in each pulse indicates the transition from closing to opening and the second line indicates the transition from opening to resting. These results show that the flow has reached a periodic steady state. Re = 4 and 12, not presented, have also reached a periodic steady state. These time-periodic solutions will be analyzed below.

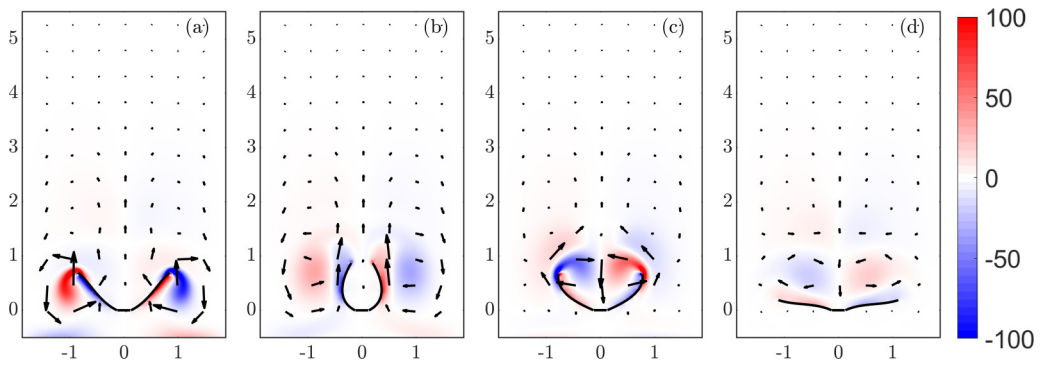

FIG. 4. The fluid flow of a pulsing soft coral at Re = 8 at (a) 10%, (b) 30%, (c) 50%, and (d) 80% of a pulse. The color map shows the vorticity and the vectors give the velocity field in the simulation. Note that these panels only present a subset of the full domain. See Supplemental Material [78] for a video of this simulation.

We observe more reversible flow, as expected, for the lower Reynolds numbers. In Figs. 5(b)–5(d), the blue solid line presents the average vertical velocity directly above the coral. There is less back flow for Re = 8 and 16 than for Re = 1 since these cases have more inertia in the flow. In Fig. 5(b) at Re = 1, the average vertical velocity two tentacle lengths above the top of the coral (red dashed line) is small in magnitude and slightly oscillates between positive and negative, mirroring the behavior directly above the coral. In Figs. 5(c) and 5(d) at Re = 8 and 16, the red dashed line remains positive and as the Reynolds number increases, the magnitude of the positive average velocity increases. Re = 16 is the only case in which the average vertical velocity four tentacle lengths above the top of the coral (yellow dotted line) is noticeably greater than zero. This shows that for Re = 8 and 16 there is a continuous upward flow away from the coral, and that as the Reynolds number increases, the magnitude of this upward flow increases. The contributions of the upward flow to the transport of oxygen away from the coral tentacles is discussed below in Sec. IV C.

The effect of the velocity boundary conditions on the flow results were also examined by conducting a study of varying domain sizes [79]. We varied both the length and width of the domain for the Re = 1 and Re = 16 cases with a coarser spatial resolution and made sure that the results

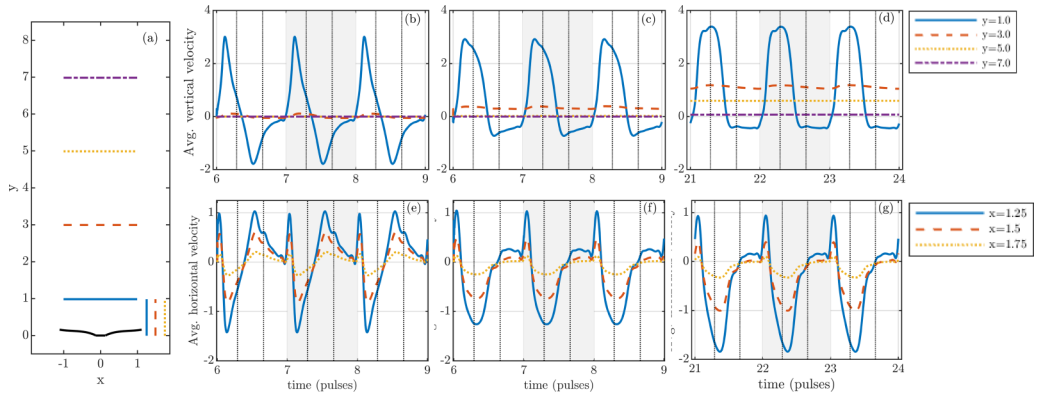

FIG. 5. Average velocities along lines at varying distances from the pulsing coral during the last three pulses of the simulations for (b, e) Re = 1, (c, f) Re = 8, and (d, g) Re = 16. (b–d) The average vertical velocities on the horizontal lines shown in panel (a). (e–g) The average horizontal velocities on the vertical lines shown in panel (a). The different colors and line styles correspond to the lines shown in panel (a).

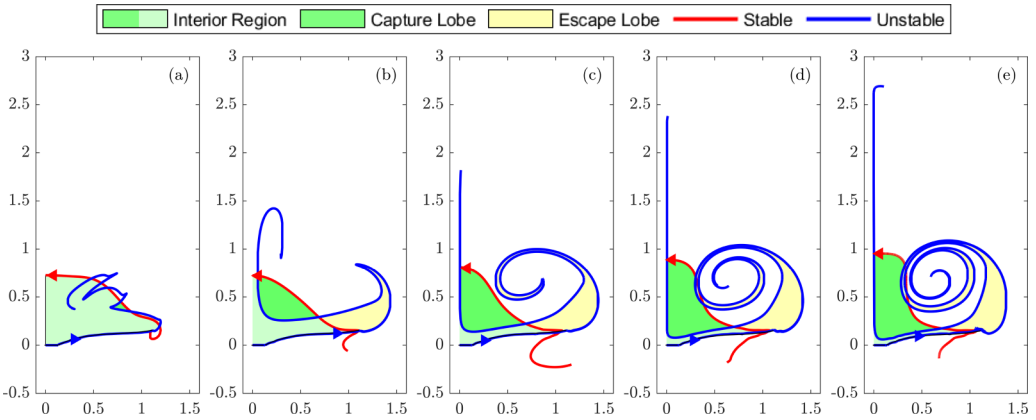

FIG. 6. Analysis of Poincaré maps for (a) Re = 1, (b) Re = 4, (c) Re = 8, (d) Re = 12, and (e) Re = 16. Half of the domain is presented. The stable manifold (red) and unstable manifold (blue) are plotted as well as the location of the tentacle (black). The interior regions, capture lobes, and escapes lobe are denoted with different colors.

presented in Fig. 5 were similar as the domain size increased. We chose the domain size such that the consecutive average velocities along the horizontal and vertical lines shown in Fig. 5(a) were not qualitatively different. The quantitative details can be found in Santiago's thesis [79].

B. Mixing analysis

Next, we quantify how the fluid flow contributes to transport away from the coral tentacles as we vary the Reynolds number. Flow trajectories are used to build a Poincaré map. This is a commonly used tool in dynamical systems to characterize the transport and mixing dynamics of fluid flow [80].

A Poincaré map tracks the location of the flow trajectories after one period. In this work, the trajectory locations are tracked at the beginning of every pulse. The trajectories are integrated using a second-order Runge-Kutta scheme, and the velocity is interpolated using a second-order interpolation scheme, commonly used in the IB method [47]. Stable and unstable invariant manifolds of the Poincaré map are computed; details of this analysis are provided in Appendix B. These manifolds define an interior and exterior region in phase space. The transport and mixing between these regions are controlled by capture and escape lobes, areas between the stable and unstable manifolds. The fluid can only pass between these regions by being mapped into or out of these lobes. The invariant manifolds and lobes of the Poincaré map provide a deeper understanding of how fluid is transported during one pulse [80].

In Fig. 6, the stable and unstable manifolds for Re = 1, 4, 8, 12, and 16 are presented. One half of the domain is plotted as the dynamics are symmetric across the y-axis. We have denoted the interior region in light and dark green and the exterior region in yellow and white. We are interested in how much fluid is leaving and entering the green region near the coral. The area of the capture lobe (dark green) is the amount of fluid that has entered the interior region (dark green and light green) from the exterior region (white and yellow) during one pulse. The area of the escape lobe (yellow) is the amount of fluid that has escaped from the interior region. Since the fluid is incompressible, the capture and escape lobes have approximately (due to numerical error) the same area. To quantify the amount of fluid replenished in the interior region over one pulse, we compute

$$\%\text{ of the fluid entering interior region} = \frac{\text{area of capture lobe}}{\text{area of interior region}} \times 100.$$

TABLE V. Area of interior regions, capture lobes, and percent of fluid entering the interior region.

Reynolds number	Area of interior region	Area of capture lobe	% of the fluid entering interior region
1	0.5485	0.0085	1.55
4	0.3790	0.1671	44.09
8	0.3581	0.2515	70.23
12	0.3648	0.2895	79.34
16	0.3816	0.3127	81.95

The results for all Reynolds numbers simulated are presented in Table V. As the Reynolds number increases the percentage of the fluid entering the interior region increases, indicating more mixing, due to the increased inertia in the flow. Note that for Re = 12 and 16, there is an overlap in the capture and escape lobes. These areas are omitted in the calculation, as we are only interested in the amount of fluid that has escaped and not re-entered the interior region.

C. Photosynthesis simulations

The photosynthesis of the symbiotic algae is modeled using an advection-diffusion equation for the byproduct oxygen. Since the pulsing coral flow has reached a quasi-steady-state and has become time periodic, the last pulse is coupled to the oxygen concentration dynamics. A more refined grid than used in the velocity simulations is needed to resolve the oxygen concentration dynamics near the tentacles. The velocity field during the final pulse for each Reynolds number is interpolated from a 250 × 600 grid onto a 500 × 1200 grid. The concentration is simulated for ten pulses, with no initial concentration in the domain. The Péclet number is varied in the concentration simulations coupled to each flow field. The Péclet numbers simulated are Pe = 1, 10, 100, 200, and 400 for both the constant and oxygen-limited photosynthesis models, for a total of 50 simulations. In Fig. 7, snapshots of the velocity field and oxygen concentration for the oxygen-limited model for Re = 8 and Pe = 100 are presented during the final pulse. Comparing these results to Fig. 4, it is clear that the vortices in the fluid flow trap the concentration and play an important role in the concentration dynamics.

In Fig. 8, the concentration dynamics for Pe = 100 at the end of the tenth pulse for varying Reynolds numbers and the two photosynthesis models are shown. For smaller Reynolds numbers,

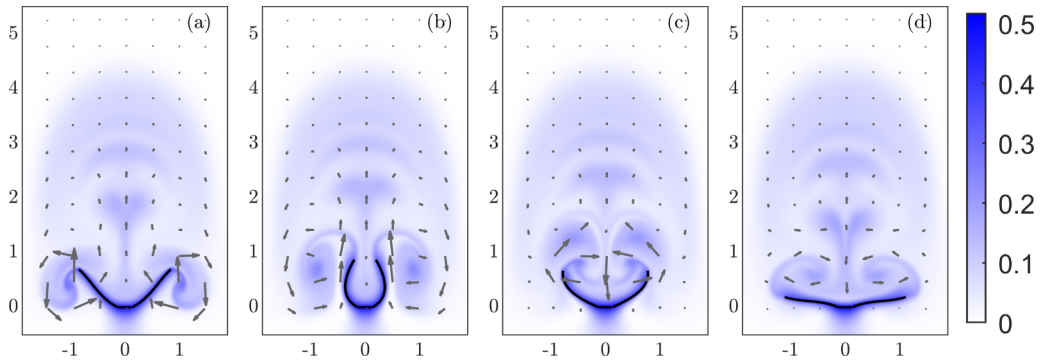

FIG. 7. The concentration dynamics of the oxygen-limited model with Re = 8 and Pe = 100 at (a) 10%, (b) 30%, (c) 50%, and (d) 80% through the tenth pulse. The vectors give the velocity field and the color map shows the oxygen concentration. Note that this panel only shows a subset of the domain. See Supplemental Material at Ref. [78] for a video of this simulation.

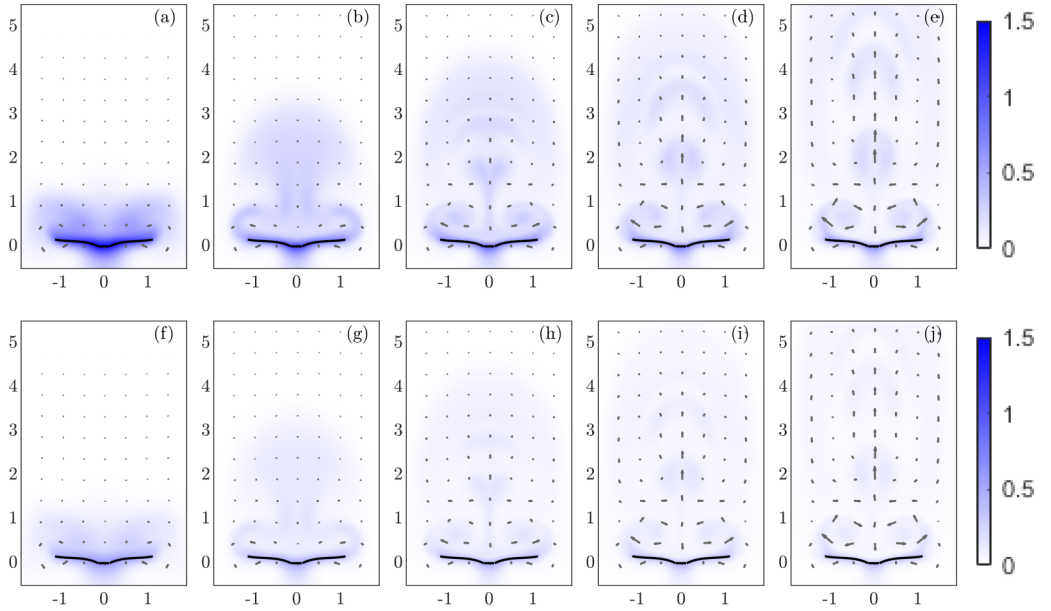

FIG. 8. The concentration dynamics at the end of ten pulses for Re = 1, 4, 8, 12, and 16 (from left to right) for Pe = 100. The color map shows the oxygen concentration for each photosynthesis model, (a–e) the constant model and (f–j) the oxygen-limited model. The vectors give the velocity field at the final time. Note that each panel only shows a subset of the domain.

the vortices do not develop and the oxygen stays in the vicinity of the coral throughout the simulation, while for larger Reynolds numbers the concentration is transported away from the coral tentacles. In these cases, the concentration is trapped in the vortices that are then pushed away from the coral. The two photosynthesis models shown here are the constant [Figs. 8(a)–8(e)] and oxygen-limited model [Figs. 8(f)–8(j)]. Since the constant model is not limited there is more oxygen present in the domain and a larger build up around the tentacles.

The interesting qualitative results observed above resulted in us conducting a more quantitative analysis of the concentration dynamics to understand the interplay between the Reynolds and Péclet numbers [79]. Here, we have presented the results for the oxygen-limited photosynthesis model; the relevant results for the constant model are similar and are omitted in this work. We computed several different quantities in each simulation: the maximum concentration to analyze the dynamics of the oxygen around the tentacles, the evaluation of the source term to quantify how much oxygen is being produced in each parameter regime, the variance in the oxygen concentration as a measure of mixing, and the transport across horizontal lines at varying heights to quantify how well the oxygen is transported away in different parameter regimes.

The maximum concentration is a metric of how much oxygen concentration builds up around the tentacles and thus indicates how well oxygen is transported away from the tentacles, less oxygen around the tentacles allows for more photosynthesis. The maximum concentration in the domain over time is presented in Figs. 9(a) and 9(b) for the oxygen-limited model. In Fig. 9(a) the Reynolds number is fixed at Re = 8 and the Péclet number is varied and in Fig. 9(b) the Péclet number is fixed at Pe = 100 and the Reynolds number is varied. The evaluation of the source term,

$$S(t) = \int_{\Gamma} \kappa(1 - C)\delta[\underline{x} - \underline{X}(s, t)]d\underline{s},$$

presented in Figs. 9(c) and 9(d), is proportional to the amount of photosynthesis occurring by the symbiotic algae in this model. This quantity allows us to study which parameters lead to more

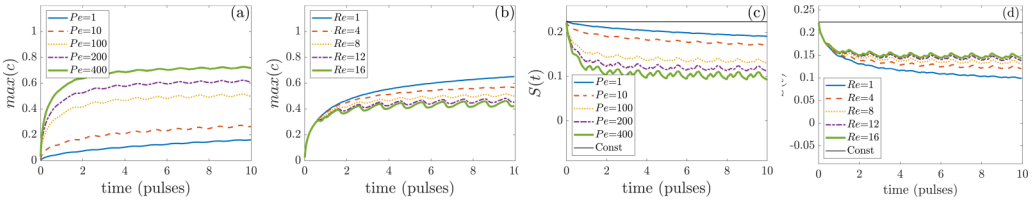

FIG. 9. The maximum concentration in the domain in the oxygen-limited model for (a) Re = 8 and varying Péclet numbers and (b) Pe = 100 and varying Reynolds numbers. Evaluation of the source term over time in the oxygen-limited model for (c) Re = 8 and varying Péclet numbers and (d) Pe = 100 and varying Reynolds numbers.

photosynthesis. Figure 9(c) presents the evaluation of the source term for Re = 8 and varying Péclet number and Fig. 9(d) presents the evaluation of the source term for Pe = 100 and varying Reynolds number for the oxygen-limited model.

In Fig. 9(a), as the Péclet number increases, the maximum concentration does too. This trend is consistent in time. Since a smaller Péclet number indicates a more diffusive driven flow, the oxygen is diffusing away from the tentacles more quickly. For a larger Péclet number, a larger accumulation of oxygen is entrained in the fluid around the tentacles. In Fig. 9(c) as the Péclet number increases, the amount of oxygen produced decreases since there is an accumulation of the concentration around the tentacle, as seen in Fig. 9(a), inhibiting the production of more oxygen. The oscillations of the evaluation of the source term for larger Péclet numbers are also consistent with the oscillations of the maximum concentration in Fig. 9(a), showing that the flow field is contributing more to the dynamics in the large Péclet number regime.

In Fig. 9(b), as the Reynolds number increases, the maximum concentration decreases. For a larger Reynolds number, with more inertia in the flow, more concentration is transported away from the coral tentacles. The maximum concentration fluctuates more in time for larger Reynolds numbers due to the periodic pulsing. Furthermore, the difference between the maximum concentrations are more pronounced in Fig. 9(a), indicating that the variations in the Péclet number contribute more significantly to the transport of oxygen away from the tentacle. In Fig. 9(d) as the Reynolds number increases, more oxygen is produced as the inertia in the fluid advects the oxygen away from the tentacles, as seen in Fig. 9(b), allowing more photosynthesis to occur.

Both quantities are reaching a quasi-steady-state in time. The maximum concentration during the final pulse is given in Fig. 10(a) and the source term is integrated in time over the tenth pulse in Fig. 10(b) for Re = 1, 4, 8, 12, and 16 and Pe = 1, 10, 100, 200, and 400. The trends shown in

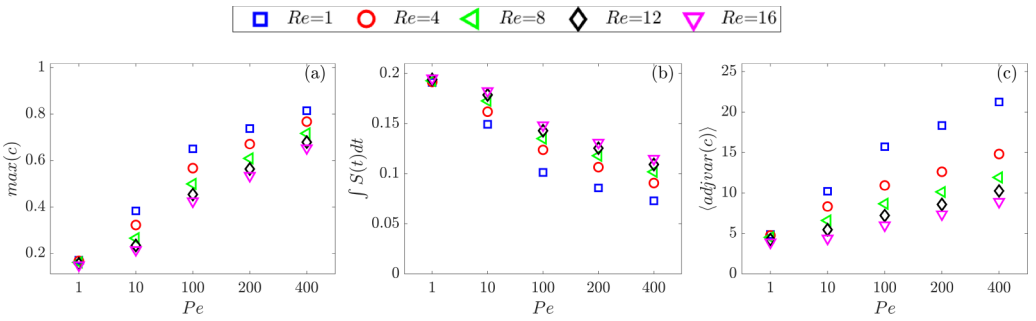

FIG. 10. (a) Maximum concentration, (b) total oxygen produced, and (c) temporal average of the adjusted concentration variance during the tenth pulse for varying Péclet and Reynolds numbers for the oxygen-limited model.

Fig. 9 over time are reflected in Fig. 10 for varying Reynolds and Péclet numbers for both quantities. One can observe that in the higher Péclet number regime, there is a benefit to increasing Reynolds number, but the benefit is not uniform. In the higher Péclet number regime, there is much more variability between Re = 1, 4, and 8, compared to Re = 8, 12, and 16, which indicates that Re = 8 is advantageous for mixing in the high Péclet number regime. The benefit from Re = 1 to 4 and Re = 4 to 8 is considerable, but there seems to be less benefit between Re = 8 and 12 and Re = 12 and 16. These larger Reynolds numbers require more energy to be expended. See discussion below. Since Re = 8 and Pe = 400 are closer to the biologically relevant parameters, these results suggest that the corals operate in a desirable mixing regime without expending extra energy.

In Fig 10, we also present the concentration variance,

$$\text{var}(c) = \sqrt{\int_\Omega [c(\underline{x}, t) - \langle c(t)\rangle]^2 d\underline{x}},$$

a measure of how mixed the system is [81]. To be able to compare between models with varying parameters and different amounts of oxygen present in the domain the adjusted variance is used,

$$\text{adj var}(c) = \sqrt{\int_\Omega \left(\frac{c(\underline{x}, t)}{\langle c(t)\rangle} - 1\right)^2 d\underline{x}}. \tag{29}$$

Ideal mixing would be when the oxygen is mixed into the domain from the tentacle to a steady state instantaneously, $c(\underline{x}, t) = \langle c(t)\rangle$ and adj var$(c) = 0$. The adjusted variance of the concentration gives a measure of how far away the solution is from this ideal mixing which takes the role of oxygen diffusion into account, unlike the analysis of the fluid flow conducted above.

The temporal average of the concentration variance during the final pulse for all Reynolds and Péclet numbers is given in Fig. 10(c). Smaller Péclet numbers have lower values of variance suggesting that diffusion is a more ideal mixer compared to advection. For larger Péclet numbers, larger Reynolds numbers have smaller values of variance. This is consistent with the previous results that indicated more mixing with larger Reynolds numbers. We see similar average adjusted variance for Re = 8, 12, and 16, and larger variance for Re = 1 and 4 in the high Péclet number regime. This indicates that the biologically relevant parameters are also advantageous for mixing in addition to photosynthesis. These results are intuitive, Figs. 10(a) and 10(b) showed that for small Péclet numbers less oxygen builds up around the tentacles resulting in more oxygen production and in the high Péclet number limit, larger Reynolds number simulations have less oxygen around the tentacles and more oxygen production. This shows that the adjusted variance metric captures the mixing trends through the lens of photosynthesis and oxygen production.

Another useful way of analyzing the photosynthesis dynamics is quantifying how far away the oxygen is transported from the coral. This metric will take into account the role of the fluid flow away from the corals, which is relevant to understanding coral colony dynamics. The previous results presented focused on the dynamics closer to the coral polyps, which are more relevant for individual polyps.

We consider a box B in the domain that spans the width of the domain, starts at $y = y_o$ and ends at the top of the domain. Then, the amount of oxygen in that box at time t is

$$c_B(y_o, t) = \int_0^t \int_{-1.875}^{1.875} c(x, y_o, t')u_2(x, y_o, t')\ dxdt',$$

considering the boundary conditions and since there is no initial oxygen in B. The limits -1.875 and 1.875 are because we are integrating over the width of the domain. This is also the total net amount of oxygen that has passed through the line $y = y_0$ by time t. To compare between simulations, the percentage of oxygen in B of the total oxygen in the domain at time t is computed as

$$\%c_B(y_o, t) = \frac{c_B(y_o, t)}{\int_\Omega c(\underline{x}, t)d\underline{x}} \times 100.$$

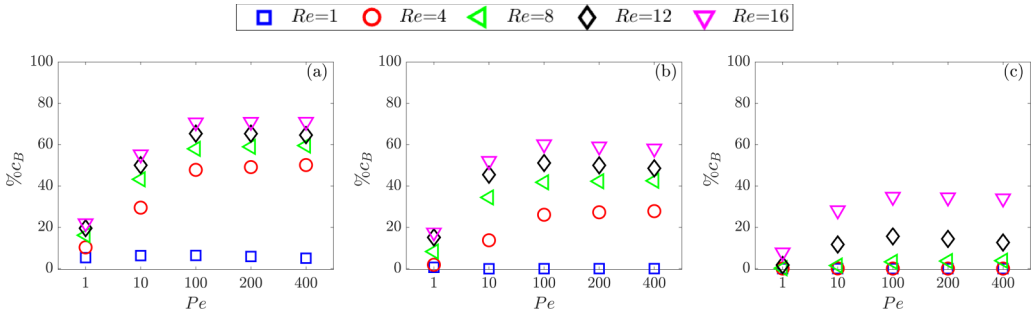

FIG. 11. Total percentage of oxygen in B at the end of the final pulse when (a) $y_o = 1$, (b) $y_o = 2$, and (c) $y_o = 4$ for varying Péclet and Reynolds numbers for the oxygen-limited model.

The long-term behavior of transport of oxygen away from the tentacles is shown in Fig. 11. The total percentage of oxygen in the box at the final time is shown for $y_o = 1$, 2, and 4 for all Reynolds and Péclet numbers. It is clear that as the Reynolds number increases, the transport away from the coral increases. The large Péclet number regime is more advective driven and is more influenced by the upward flow than smaller Péclet numbers, which diffuse quickly away from the coral tentacles but are not transported upward. The transport upward rather than diffusive driven radial transport could be advantageous for coral colonies as there could be less recirculation of oxygen-rich water by neighboring polyps. In Fig. 11(a) for $y_o = 1$, we can see more variability between Re = 1 and 4, and much less variability between Re = 4, 8, 12, and 16, indicating that Re = 4 is advantageous for transporting oxygen a short distance. Similarly, Fig. 11(b) shows that Re = 8 is advantageous for transporting up to a coral tentacle length away and Fig. 11(c) shows Re =16 is advantageous for transporting oxygen up to three coral tentacle lengths away. From the previous analysis, we know that Re = 8 is advantageous for mixing and more photosynthesis, so this indicates that transporting oxygen a tentacle length away is enough to facilitate the photosynthesis and prevent fluid recirculation by neighboring polyps.

In this section, we have shown results of the pulsing coral fluid flow coupled tothe photosynthesis model. The mixing due to the flow was examined for varying Reynolds numbers in Sec. IV B. The photosynthesis model was quantitatively analyzed for varying Reynolds and Péclet numbers by observing the maximum oxygen concentration, the evaluation of the oxygen-limited source term, the adjusted variance of the oxygen concentration, and the transport of oxygen away from the coral tentacles.

We have studied the dynamics as we kept the Reynolds number fixed and varied the Péclet number and vice versa. When both numbers are simultaneously varied this is equivalent to varying the Schmidt number $Sc = \frac{\nu}{D}$, the ratio of fluid viscosity to diffusivity. We have chosen to focus on the Reynolds and Péclet numbers as the resulting trends were more clear. By analyzing these results, we have found advantageous parameter regimes for mixing, photosynthesis, and oxygen transport.

We now investigate the energy expended by the coral in different Reynolds number regimes. The nondimensional energy at time t^n is computed using

$$E^n = \frac{\kappa_T}{2} \sum_{k=1}^{N} \left(\left\| \underline{X}_k^n - \underline{X}_{Tk}^n \right\|_2 \right)^2.$$

This is the energy functional corresponding to the tether points not accounting for the spring damping present in Eq. (5). The damping in Eq. (5) was included to provide numerical stability rather than for physical modeling and therefore is omitted in the energy study here. Furthermore, the damping forces are small in magnitude compared to the tether forces, so they do not affect the energy significantly.

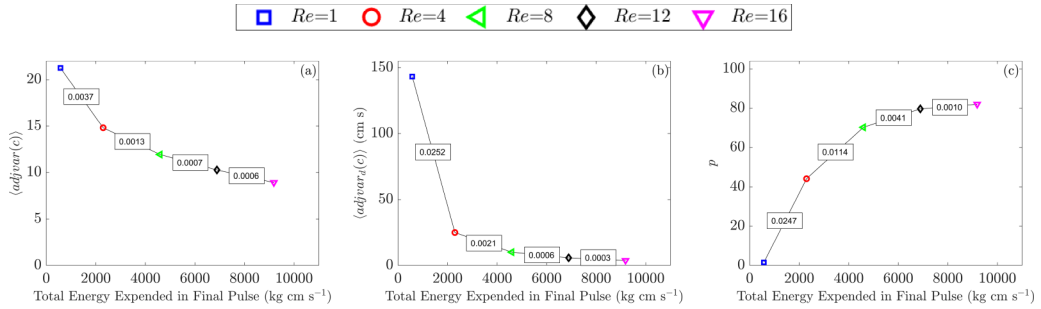

FIG. 12. (a) Nondimensional average variance, (b) dimensional average variance, and (c) percentage of fluid entering the interior region as a function of the total dimensional energy expended during the final pulse for Pe = 400. The corresponding colors and shapes give the corresponding Reynolds number. The text boxes give the magnitude of the corresponding rate of change.

Using the dimensional energies allows a better understanding of the role of the Reynolds number in the energy expended by the coral. To dimensionalize the energy we define $\tilde{\kappa}_T = \kappa_T \rho L^3 f^2$, where L is the tentacle length, f is the pulsing frequency, and ρ is the fluid density. We also dimensionalize the tentacles positions as $\tilde{\underline{X}} = \underline{X}L$ and tether point positions as $\tilde{\underline{X}}_T = \underline{X}_T L$. Thus the dimensionalized energy at time t^n is

$$\tilde{E}^n = \frac{\tilde{\kappa}_T}{2} \sum_{k=1}^{N} \left(\left\| \tilde{\underline{X}}_k^n - \tilde{\underline{X}}_{T\,k}^n \right\|_2 \right)^2 = \frac{\kappa_T \rho L^3 f^2}{2} \sum_{k=1}^{N} \left(\left\| \underline{X}_k^n L - \underline{X}_{T}{}_k^n L \right\|_2 \right)^2.$$

We considered the total energy expended in the final pulse,

$$\text{Total energy} = \int_9^{10} \tilde{E} dt,$$

computed using the trapezoidal rule.

In Figs. 12(a) and 12(b) we show the average adjusted variance of the oxygen concentration in the domain and in Fig. 12(c) the percentage of fluid leaving the interior region in the final pulse from Table V as a function of the dimensionalized total energy expended for Pe = 400. Figure 12(a) shows the temporal average variance, Eq. (29), over the final pulse in dimensionless form, $\langle \text{adj var}(c) \rangle = \int_9^{10} \text{adj var}(c) dt$. Figure 12(b) shows the temporal average variance over the final pulse in dimensional form, $\langle \text{adj var}_d(c) \rangle = \frac{1}{f} \int_9^{10} \sqrt{\int_\Omega (\frac{c(\underline{x},t)}{\langle c(t) \rangle} - 1)^2 d\underline{x} L^2} dt$. The corresponding Reynolds numbers for the energies computed are denoted, and the magnitude of the rate of change is given. We see that with increasing Reynolds number, the energy is increasing uniformly, but the benefit is not. One can observe that the magnitude of the rate of change decreases with increasing energy. In particular, one can observe a benefit from Re = 1 and 4 and from Re = 4 and 8, with very little benefit after Re = 8.

Figure 13 ties together the fluid flow mixing analysis and oxygen concentration results. The oxygen concentration after ten pulses for Pe = 100 and 400 and varying Reynolds numbers are shown overlaid with the corresponding stable and unstable manifolds of the fluid flow. The higher Péclet number regime shows better agreement between the Poincaré map manifolds and the oxygen dynamics, as expected. For Re = 1, most of the oxygen stays within the interior region and is not transported away. For the larger Reynolds numbers, the oxygen moves out of the interior region, into the escape lobe (which corresponds to the vortices in the flow), and into other subsequent lobes in the domain. The effect of diffusion and the source term on these dynamics can be observed. In these results the Péclet number is constant in Figs. 13(a)–13(e) and Figs. 13(f)–13(j). However, if the Péclet number had been defined using the maximum flow velocity, rather than the pulsing

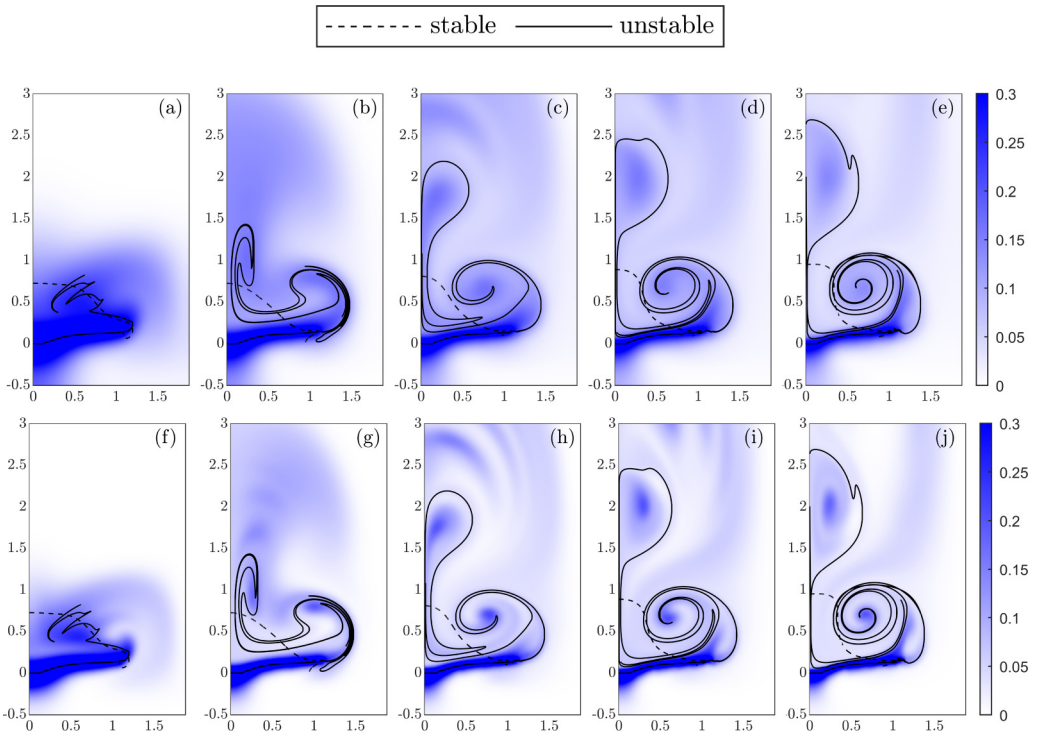

FIG. 13. Oxygen concentration for the oxygen-limited photosynthesis model at the end of ten pulses for (a–e) Pe = 100 (f–j) Pe = 400 for varying Reynolds numbers, (a, f) Re = 1, (b, g) Re = 4, (c, h) Re = 8, (d, i) Re = 12, and (e, j) Re = 16, overlaid with the corresponding stable (dashed) and unstable (solid) manifolds. Half of the domain is presented.

frequency, then Figs. 13(a) and 13(f) would have a smaller Péclet number than Figs. 13(e) and 13(j). In these dynamics, Figs. 13(a) and 13(f) are clearly more diffusive, and therefore the manifolds do not give as much information as in Figs. 13(e) and 13(j). The algae produces oxygen on both sides of the tentacle. The oxygen produced from the underside of the tentacle is not in the interior region, so the oxygen dynamics can only partially be explained by the Poincaré map lobes. This shows that it is necessary to model the concentration dynamics to understand how the mixing facilities the photosynthesis of the symbiotic algae. However, both techniques provide useful and relevant information into the mixing dynamics of the pulsing soft corals and the photosynthesis of their symbiotic algae.

V. DISCUSSION AND CONCLUSIONS

In this work a new mathematical model and numerical method is developed to study the fluid flow of a pulsing soft coral coupled with the photosynthesis of symbiotic algae. The fluid flow of the pulsing soft corals was solved for using the immersed boundary method and the photosynthesis was modeled by solving an advection-diffusion equation for oxygen, the byproduct of photosynthesis. Included in the advection-diffusion equation is a source term on the moving tentacles to model the production of oxygen by the symbiotic algae. The mixing due to fluid flow was analyzed using a dynamical systems approach by applying lobe dynamics theory. The photosynthesis and mixing dynamics were quantitatively analyzed using the maximum oxygen concentration, the evaluation of the oxygen-limited source term, the adjusted variance of the oxygen concentration, and the transport of oxygen away from the coral tentacles for varying Reynolds and Péclet numbers. The novelty of

this work was including a photosynthesis model coupled with a fluid-structure interaction. This required the development of a numerical method to solve a partial differential equation with a boundary condition on a moving immersed elastic boundary.

In the analysis of the fluid flow, the larger Reynolds numbers produced more mixing, as expected. The benefit from larger Reynolds number lessens right around the biologically relevant Reynolds number, which is determined by the kinematics of the pulsing coral. We found that the energy expended in the higher Reynolds number regimes increased uniformly but the mixing benefit did not. The other primary numerical study on soft coral flow dynamics around a single coral polyp used Lagrangian Coherent Structures and Finite Time Lyapunov exponents to examine mixing [36]. Similar methodology was presented on PIV flow fields to study the feeding habits of jellyfish [15]. These methods are useful for qualitative analysis for regions of high or low mixing in unsteady flow. The methodology presented in this paper instead is able to give quantitative results for varying Reynolds numbers. This allows for a more objective interpretation of the mixing benefit due to the flow by giving a metric of how much mixing is occurring, rather than just where the mixing is occurring.

The metrics used to analyze the photosynthesis dynamics showed increased mixing and more oxygen production for smaller Péclet numbers. In this regime the oxygen concentration diffuses away from the tentacles and allows for more mixing and less buildup of oxygen concentration around the tentacles. These results were similar for all simulated Reynolds numbers. However, the biologically relevant Péclet number for dissolved oxygen in water is large, $O(100)$–$O(1000)$. In this regime the fluid flow plays a significant role. Smaller Reynolds numbers resulted in less mixing and photosynthesis due to the reversible flow, while the increased inertia of the larger Reynolds number allowed for more mixing and more photosynthesis. This benefit of larger Reynolds number was not uniform, after $\mathrm{Re} = 8$ the benefit was considerably less. This indicates that the biologically relevant Reynolds number, $\mathrm{Re} \approx 8$, is advantageous for mixing and photosynthesis in a larger Péclet regime, suggesting that these corals are expending the minimal energy required to gain the most benefit. The energy expended after $\mathrm{Re} = 8$ increased linearly, but we can observe the benefit diminishing. We expect these corals to respond to evolutionary pressure to either obtain a specific body size range or pulse with a frequency that gives advantageous mixing. Note that increasing size or frequency increases the Péclet number, decreasing mixing and photosynthesis, and increases the Reynolds number, increasing mixing and photosynthesis, so the right balance must be found taking the energy expended into account.

The role of fluid flow and diffusion in capture mechanisms of appendages, such as feeding or olfaction, has been well studied [16–18,82,83]. It is widely accepted that although the appendages bring the materials close to the desired location, the actual capture is dominated by the diffusion dynamics [82]. This work focuses on expelling a photosynthetic byproduct because it is unlikely that the corals' main energy source is from filter-feeding, a capturing process [35]. We can expect these dynamics to be similar, where diffusion dominates the dynamics near the tentacle. After the diffusion has transported the oxygen a short distance away from the tentacle, the fluid can transport the oxygen farther away from the coral. Instead in Fig. 13, we observe that the fluid dynamics do affect the concentration close to the tentacles. As the Reynolds number increases, the width of the oxygen buildup around the tentacle decreases. The increased inertia in the fluid flow is removing oxygen by thinning the width of the accumulated oxygen around the tentacle. Thus both advective and diffusive forces can be significant in the dynamics close to appendages.

The next step of this work is to apply this methodology in three dimensions. We expect the trends and intuition developed by this two-dimensional study to be present in the three-dimensional results. However, we already know that the fluid flow has characteristics that cannot be captured in two dimensions [36]. These methods will be implemented in the software library IBAMR [60]. The computational expense of the simulations presented here resulted in limitations in the parameter studies. To run simulations with larger Reynolds numbers, larger domains are needed and simulations would have to be run for longer times to reach a periodic steady state. Larger Péclet numbers would have required a more refined mesh to resolve the solution close to the tentacles.

IBAMR has support for parallelization and adaptive meshes allowing for the ability to sample a larger parameter space.

Once this methodology is implemented in three dimensions, many different experimental studies can be done with numerical studies to validate and elucidate some other research questions. Kremien *et al.* looked at the role of pulsing in photosynthesis and photorespiration in varying ambient oxygen levels and light intensity [35]. Dye visualization around live or model corals could be used to observe how the fluid is swept away from the coral tentacles with corresponding numerical studies. Both methods can be used to cross-validate the results. In laboratory settings, these corals are known to filter feed [84]. Quantitative experiments could be used to investigate the benefit of filter-feeding and whether the coral kinematics change to enhance feeding efficiency. An interesting experiment could also be changing the light irradiance or artificially heightening or lowering the carbon dioxide levels around live corals and observing and quantifying any change in the pulsing behavior as it is known that photosynthesis rates vary in coral reef organisms with light irradiance [85].

Another avenue to be explored is the role of background flow on the corals. The coral colonies are located in areas with significant background flow, and understanding how the intensity of the background flow affects the local and colony dynamics is nontrivial. The flow over pulsing colonies is up to an order of magnitude more turbulent than nonpulsing colonies [35]. Our work can be extended to investigate the effect of various background flows on the photosynthesis of a nonpulsing polyp. Additionally, one could introduce turbulence in the background flow to understand how much turbulence is needed to achieve the same effect as the pulsing.

Further, the methods and analysis provided here can be used in industrial and engineering applications where a pumping, pulsing, or stirring mechanism is used to facilitate mixing. They can also be used to analyze photosynthesis and mass transfer in other biological systems.

ACKNOWLEDGMENTS

Funding for this research was provided by the National Science Foundation, Grants No. PHY-1505061 and No. DMS-1853608. The numerical simulations conducted in this work were performed on the MERCED cluster at the University of California, Merced, funded by the National Science Foundation, Grant No. NSF ACI-1429783. K.A.M. acknowledges funding from the National Science Foundation, Grant No. NSF CMMI-1825379. The authors thank Laura A. Miller for contributing to several discussions on this project.

APPENDIX A: KINEMATIC MOTION OF CORAL

The kinematic motion of the corals mentioned in Sec. II is discussed here. Experimental video of pulsing soft coral was used to find the motion of the coral tentacles [36]. Six points were tracked on one tentacle at every frame of five different coral polyps for five pulses. At each frame, polynomials were fit using the position of the six points. Then, the coefficients of these polynomials were nondimensionalized and averaged over the different polyps and pulses. Finally, time-dependent polynomials were fit to these coefficients. The position of the tether points are then given by

$$X_T(s,t) = C_3(t)s^3 + C_2(t)s^2 + C_1(t)s + C_0(t), \tag{A1}$$

$$Y_T(s,t) = D_3(t)s^3 + D_2(t)s^2 + D_1(t)s + D_0(t), \tag{A2}$$

with the time-dependent coefficients C_i(t) and $D_i(t)$ for the data a_{ji} and b_{ji} given by

$$C_i(t) = b_{4i}t^4 + b_{3i}t^3 + b_{2i}t^2 + b_{1i}t + b_{0i}, \tag{A3}$$

$$D_i(t) = a_{4i}t^4 + a_{3i}t^3 + a_{2i}t^2 + a_{1i}t + a_{0i}. \tag{A4}$$

To model the coral movement in two-dimensions, two tentacles are included and it is assumed that the motion of each tentacle is a reflection of the other, as shown in Fig. 1 in the main text.

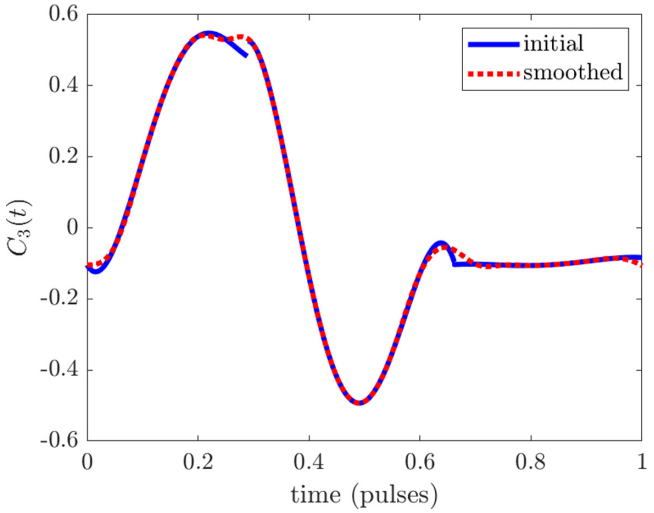

FIG. 14. Example of coefficient $C_3(t)$ from experimental data (blue) and the smoothed fit used in the modeling (red).

In the collected experimental data the coefficients have slight discontinuities in the coral motion and furthermore prescribe an initial velocity inconsistent to the assumption that the fluid is initially at rest. To remedy these issues an equally spaced sample of each coefficient was taken, and then a curve was fit through the sample using clamped splines, enforcing continuity and a zero initial velocity to get consistent initial conditions, as shown in Fig. 14 for one coefficient.

APPENDIX B: POINCARÉ MAP MANIFOLDS

The method to compute the manifolds of the Poincaré maps introduced in Sec. IV B is discussed here. To find the stable manifold, a fixed point on the separatrix ($x = 0$) was computed and a thin horizontal line of points were initialized at the fixed point. The points were mapped backwards in time to compute the stable manifold using second-order Runge Kutta and a second-order interpolation scheme used in the immersed boundary method [47]. The tentacles are known to generate the unstable manifold. Points were initialized along the tentacle. The points were mapped forward in time to compute the unstable manifold. In computing both the stable and unstable manifold for each Reynolds number simulation, the number of points initialized and the number of iterations forwards or backwards in time were adjusted empirically.

[1] T. Y. Wu, Fish swimming and bird/insect flight, Annu. Rev. Fluid Mech. **43**, 25 (2011).
[2] H. Liu, Simulation-based biological fluid dynamics in animal locomotion, Appl. Mech. Rev. **58**, 269 (2005).
[3] P. W. Webb, Body form, locomotion and foraging in aquatic vertebrates, American Zoologist **24**, 107 (1984).
[4] M. J. Lighthill, Aquatic animal propulsion of high hydromechanical efficiency, J. Fluid Mech. **44**, 265 (1970).
[5] R. Godoy-Diana and B. Thiria, On the diverse roles of fluid dynamic drag in animal swimming and flying, J. R. Soc., Interface **15**, 20170715 (2018).
[6] L. A. Miller and C. S. Peskin, A computational fluid dynamics of "clap and fling" in the smallest insects, J. Exp. Biol. **208**, 195 (2005).

[7] H. Liu, S. Ravi, D. Kolomenskiy, and H. Tanaka, Biomechanics and biomimetics in insect-inspired flight systems, Philos. Trans. R. Soc. B **371**, 20150390 (2016).
[8] J. O. Dabiri, Renewable fluid dynamic energy derived from aquatic animal locomotion, Bioinspir. Biomim. **2**, L1 (2007).
[9] M. S. Triantafyllou and G. S. Triantafyllou, An efficient swimming machine, Sci. Am. **272**, 64 (1995).
[10] G. V. Lauder and E. G. Drucker, Forces, fishes, and fluids: Hydrodynamic mechanisms of aquatic locomotion, Physiology **17**, 235 (2002).
[11] I. K. Bartol, P. S. Krueger, J. T. Thompson, and W. J. Stewart, Swimming dynamics and propulsive efficiency of squids throughout ontogeny, Integr. Comp. Biol. **48**, 720 (2008).
[12] H. U. Riisgård and P. S. Larsen, Particle capture mechanisms in suspension-feeding invertebrates, Mar. Ecol. Prog. Ser. **418**, 255 (2010).
[13] S. Van Wassenbergh and P. Aerts, Rapid pivot feeding in pipefish: flow effects on prey and evaluation of simple dynamic modeling via computational fluid dynamics, J. R. Soc., Interface **5**, 1291 (2008).
[14] J. R. N. Lazier and K. H. Mann, Turbulence and the diffusive layers around small organisms, Deep Sea Res. Part A. Oceanogr. Res. Papers **36**, 1721 (1989).
[15] J. Peng and J. O. Dabiri, Transport of inertial particles by Lagrangian coherent structures: Application to predator-prey interaction in jellyfish feeding, J. Fluid Mech. **623**, 75 (2009).
[16] L. Waldrop, M. Reidenbach, and M. Koehl, Flexibility of crab chemosensory sensilla enables flicking antennules to sniff, Biol. Bull. **229**, 185 (2015).
[17] L. D. Waldrop, L. A. Miller, and S. Khatri, A tale of two antennules: The performance of crab odour-capture organs in air and water, J. R. Soc., Interface **13**, 20160615 (2016).
[18] L. D. Waldrop, Y. He, and S. Khatri, What can computational modeling tell us about the diversity of odor-capture structures in the pancrustacea? J. Chem. Ecol. **44**, 1084 (2018).
[19] R. Stocker and J. R. Seymour, Ecology and physics of bacterial chemotaxis in the ocean, Microbiol. Mol. Biol. Rev. **76**, 792 (2012).
[20] C. E. López, A. Théry, and E. Lauga, A stochastic model for bacteria-driven micro-swimmers, Soft Matter **15**, 2605 (2019).
[21] R. Dillon, L. Fauci, and D. Gaver, A microscale model of bacterial swimming, chemotaxis and substrate transport, J. Theor. Biol. **177**, 325 (1995).
[22] J. R. Seymour, R. Simó, T. Ahmed, and R. Stocker, Chemoattraction to dimethylsulfoniopropionate throughout the marine microbial food web, Science (NY) **329**, 342 (2010).
[23] S. D. Olson, Fluid dynamic model of invertebrate sperm chemotactic motility with varying calcium inputs, J. Biomech. **46**, 329 (2013).
[24] A. Kiselev and L. Ryzhik, Biomixing by chemotaxis and enhancement of biological reactions, Commun. Partial Diff. Equ. **37**, 298 (2012).
[25] J. F. Jikeli, L. Alvarez, B. M. Friedrich, L. G. Wilson, R. Pascal, R. Colin, M. Pichlo, A. Rennhack, C. Brenker, and U. B. Kaupp, Sperm navigation along helical paths in 3d chemoattractant landscapes, Nat. Commun. **6**, 7985 (2015).
[26] R. K. Zimmer and J. A. Riffell, Sperm chemotaxis, fluid shear, and the evolution of sexual reproduction, Proc. Natl. Acad. Sci. U.S.A. **108**, 13200 (2011).
[27] J. P. Bitog, I. B. Lee, C. G. Lee, K. S. Kim, H. S. Hwang, S. W. Hong, I. H. Seo, K. S. Kwon, and E. Mostafa, Application of computational fluid dynamics for modeling and designing photobioreactors for microalgae production: A review, Comput. Electr. Agric. **76**, 131 (2011).
[28] T. Mass, A. Genin, U. Shavit, M. Grinstein, and D. Tchernov, Flow enhances photosynthesis in marine benthic autotrophs by increasing the efflux of oxygen from the organism to the water, Proc. Natl. Acad. Sci. U.S.A. **107**, 2527 (2010).
[29] W. C. Dennison and D. J. Barnes, Effect of water motion on coral photosynthesis and calcification, J. Exp. Mar. Biol. Ecol. **115**, 67 (1988).
[30] O. H. Shapiro, V. I. Fernandez, M. Garren, J. S. Guasto, F. P. Debaillon-Vesque, E. Kramarsky-Winter, A. Vardi, and R. Stocker, Vortical ciliary flows actively enhance mass transport in reef corals, Proc. Natl. Acad. Sci. U.S.A. **111**, 13391 (2014).

[31] M. M. Hossain and A. E. Staples, Passive vortical flows enhance mass transport in the interior of a coral colony, Phys. Fluids **31**, 061701 (2019).
[32] Y. Gabay, Y. Benayahu, and M. Fine, Does elevated $p\mathrm{co}_2$ affect reef ocotocorals? Ecol. Evol. **3**, 465 (2013).
[33] P.-J. Sung, M.-R. Lin, M. Y. Chiang, and T.-L. Hwang, Soft corals and sea fans, Bull. Chem. Soc. Jpn. **82**, 987 (2009).
[34] K. Fabricius and D. Klumpp, Widespread mixotrophy in reef-inhabiting soft corals: The influence of depth, and colony expansion and contraction on photosynthesis, Mar. Ecol. Prog. Ser. **125**, 195 (1995).
[35] M. Kremien, U. Shavit, T. Mass, and A. Genin, Beneft of pulsation in soft corals, Proc. Natl. Acad. Sci. U.S.A. **110**, 8978 (2013).
[36] J. E. Samson, L. A. Miller, D. Ray, R. Holzman, U. Shavit, and S. Khatri, A novel mechanism of mixing by pulsing corals, J. Exp. Biol. **222**, 15 (2019).
[37] J. E. Samson and L. A. Miller, Collective pulsing in xeniid corals: Part II—Using computational fluid dynamics to determine if there are benefits to coordinated pulsing, Bull. Math. Biol. **82**, 67 (2020).
[38] T. P. Chiang, W. H. Sheu, and R. R. Hwang, Effect of Reynolds number on the eddy structure in a lid-driven cavity, Int. J. Numer. Methods Fluids **26**, 557 (1998).
[39] E. Guilmineau and P. Queutey, A numerical simulation of vortex shedding from an oscillating circular cylinder, J. Fluids Struct. **16**, 773 (2002).
[40] I. Jadic, R. So, and M. Mignolet, Analysis of fluid-structure interactions using a time-marching technique, J. Fluids Struct. **12**, 631 (1998).
[41] R. D. Moser, J. Kim, and N. N. Mansour, Direct numerical simulation of turbulent channel flow up to Re=590, Phys. Fluids **11**, 943 (1999).
[42] A. M. Tartakovsky and S. P. Neuman, Effects of Peclet number on pore-scale mixing and channeling of a tracer and on directional advective porosity, Geophys. Res. Lett. **35**, L21401 (2008).
[43] S. Michelin and E. Lauga, Phoretic self-propulsion at finite Péclet numbers, J. Fluid Mech. **747**, 572 (2014).
[44] R. B. Fdhila and P. C. Duineveld, The effect of surfactant on the rise of a spherical bubble at high Reynolds and Peclet numbers, Phys. Fluids **8**, 310 (1996).
[45] S. Ubal, C. H. Harrison, P. Grassia, and W. J. Korchinsky, Numerical simulation of mass transfer in circulating drops, Chem. Eng. Sci. **65**, 2934 (2010).
[46] N. Kishore, R. P. Chhabra, and V. Eswaran, Mass transfer from ensembles of Newtonian fluid spheres at moderate Reynolds and Peclet numbers, Chem. Eng. Res. Des. **85**, 1203 (2007).
[47] C. S. Peskin, The immersed boundary method, Acta Numer. **11**, 479 (2002).
[48] C. S. Peskin, Flow patterns around heart valves: A numerical method, J. Comput. Phys. **10**, 252 (1972).
[49] B. E. Griffith, Immersed boundary model of aortic heart valve dynamics with physiological driving and loading conditions, Int. J. Numer. Meth. Biomed. Engng. **28**, 317 (2012).
[50] A. Baird, L. Waldrop, and L. Miller, Neuromechanical pumping: Boundary flexibility and traveling depolarization waves drive flow within valveless, tubular hearts, Jpn. J. Ind. Appl. Math. **32**, 829 (2015).
[51] R. P. Beyer, A computational model of the cochlea using the immersed boundary method, J. Comput. Phys. **98**, 145 (1992).
[52] L. J. Fauci and A. McDonald, Sperm motility in the presence of boundaries, Bull. Math. Biol. **57**, 679 (1995).
[53] L. J. Fauci and C. S. Peskin, A computational model of aquatic animal, J. Comput. Phys. **77**, 85 (1988).
[54] G. Herschlag and L. Miller, Reynolds number limits for jet propulsion: A numerical study of simplified jellyfish, J. Theor. Biol. **285**, 84 (2011).
[55] C. Tu and C. S. Peskin, Stability and instability in the computation of flows with moving immersed boundaries: A comparison of three methods, SIAM J. Sci. Stat. Comput. **13**, 1361 (1992).
[56] D. Goldstein, R. Handler, and L. Sirovich, Modeling a no-slip flow boundary with an external force field, J. Comput. Phys. **105**, 354 (1993).
[57] M. C. Lai and C. S. Peskin, An immersed boundary method with formal second-order accuracy and reduced numerical viscosity, J. Comput. Phys. **160**, 705 (2000).

[58] J. M. Teran and C. S. Peskin, Tether force constraints in Stokes flow by the immersed boundary method on a periodic domain, SIAM J. Sci. Comput. **31**, 3404 (2009).
[59] K. Y. Chen, K. A. Feng, Y. Kim, and M. C. Lai, A note on pressure accuracy in immersed boundary method for Stokes flow, J. Comput. Phys. **230**, 4377 (2011).
[60] B. E. Griffith, R. D. Hornung, D. M. McQueen, and C. S. Peskin, An adaptive, formally second order accurate version of the immersed boundary method, J. Comput. Phys. **223**, 10 (2007).
[61] Y. Bao, A. Donev, B. E. Griffith, D. M. McQueen, and C. S. Peskin, An immersed boundary method with divergence-free velocity interpolation and force spreading, J. Comput. Phys. **347**, 183 (2017).
[62] B. E. Griffith, On the volume conservation of the immersed boundary method, Commun. Comput. Phys. **12**, 401 (2012).
[63] Y. Kim and C. S. Peskin, Penalty immersed boundary method for an elastic boundary with mass, Phys. Fluids **19**, 053103 (2007).
[64] Y. Liu and Y. Mori, Properties of discrete delta functions and local convergence of the immersed boundary method, SIAM J. Numer. Anal. **50**, 2986 (2012).
[65] Y. Mori, Convergence proof of the velocity field for a stokes flow immersed boundary method, Commun. Pure Appl. Math. **61**, 1213 (2008).
[66] K. Y. Chen and M. C. Lai, A conservative scheme for solving coupled surface-bulk convection-diffusion equations with an application to interfacial flows with soluble surfactant, J. Comput. Phys. **257**, 1 (2014).
[67] M. M. Hopkins and L. J. Fauci, A computational model of the collective fluid dynamics of motile micro-organisms, J. Fluid Mech. **455**, 149 (2002).
[68] A. Chorin, Numerical solution of the Navier-Stokes equations, Math. Comput. **22**, 745 (1968).
[69] L. J. P. Timmermans, P. D. Minev, and F. N. Van De Vosse, An approximate projection scheme for incompressible flow using spectral elements, Int. J. Numer. Methods Fluids **22**, 673 (1996).
[70] J. L. Guermond and J. Shen, On the error estimates for the rotational pressure-correction projection methods, Math. Comput. **73**, 1719 (2004).
[71] L. Klinteberg, D. Lindbo, and A. K. Tornberg, An explicit Eulerian method for multiphase flow with contact line dynamics and insoluble surfactant, Comput. Fluids **101**, 50 (2014).
[72] S.-G. Cai, A. Ouahsine, H. Smaoui, J. Favier, and Y. Hoarau, An efficient implicit direct forcing immersed boundary method for incompressible flows, J. Phys.: Conf. Ser. **574**, 012165 (2015).
[73] F. Harlow and J. Welch, Numerical calculation of time-dependent viscous incompressible flow of fluid with free surface, Phys. Fluids **8**, 2182 (1965).
[74] J. M. Stockie and B. R. Wetton, Analysis of stiffness in the immersed boundary method and implications for time-stepping schemes, J. Comput. Phys. **154**, 41 (1999).
[75] G. Strang, On the construction and comparison of difference schemes, SIAM J. Numer. Anal. **5**, 506 (1968).
[76] X.-D. Liu, S. Osher, T. Chan *et al.*, Weighted essentially nonoscillatory schemes, J. Comput. Phys. **115**, 200 (1994).
[77] Y. Liu and Y. Mori, Lp convergence of the immersed boundary method for stationary Stokes problems, SIAM J. Numer. Anal. **52**, 496 (2014).
[78] See Supplemental Material at http://link.aps.org/supplemental/10.1103/PhysRevFluids.7.033102 for a video simulation of Figs. 4 and 7.
[79] M. Santiago, Numerical methods for modeling the fluid flow of pulsing soft corals and the photosynthesis of their symbiotic algae, Ph.D. thesis, University of California, Merced, 2021.
[80] J. Meiss, Thirty years of turnstiles and transport, Chaos **25**, 097602 (2015).
[81] W. Liu and G. Haller, Strange eigenmodes and decay of variance in the mixing of diffusive tracers, Physica D: Nonlin. Phenom. **188**, 1 (2004).
[82] M. A. R. Koehl, *Hydrodynamics of Sniffing by Crustaceans* (Springer, New York, 2011), pp. 85–102.
[83] M. Koehl, The fluid mechanics of arthropod sniffing in turbulent odor plumes, Chem. Senses **31**, 93 (2006).
[84] L. Miller and J. Samson (private communication) (2016).
[85] Y. Sawall and E. J. Hochberg, Diel versus time-integrated (daily) photosynthesis and irradiance relationships of coral reef organisms and communities, PLoS ONE **13**, e0208607 (2018).